

CHF mechanism in flow boiling from a short heated wall—II. Theoretical CHF model

J. E. GALLOWAY† and I. MUDAWAR‡

Boiling and Two-Phase Flow Laboratory, School of Mechanical Engineering, Purdue University,
West Lafayette, IN 47907, U.S.A.

(Received 11 May 1992 and in final form 1 December 1992)

Abstract—A theoretical CHF model is presented which is based upon the flow visualization of the wavy liquid–vapor interface near the heated surface as reported in Part I of this study. At approximately 90% of CHF, bubbles coalesced into a continuous wavy vapor layer and vigorous boiling was observed in a liquid sub-film beneath the vapor layer. This efficient boiling mechanism was transformed to boiling at isolated regions, wetting fronts, at approximately 95% of CHF. Wetting fronts were established when minimum points in the wavy vapor interface made contact with the heater surface. Regions surrounding the wetting fronts remained dry as the supply of liquid was consumed. CHF was triggered by intense vapor production which lifted the upstream wetting front away from the heater surface, cutting the supply of liquid locally and causing the heat flux to become more concentrated at the remaining wetting fronts. Soon after, remaining wetting fronts were also lifted from the heater surface and the surface temperature increased more rapidly. The new mechanistic CHF model incorporates classical interfacial instability theory for a confined two-dimensional wave, a separated two-phase flow model and a criterion for separation of the liquid–vapor interface from the heater surface. The model predictions show good agreement with the experimental data.

1. INTRODUCTION

MOST CHF models are based on a description of a limiting process that restricts liquid flow to the heated surface during intense boiling. CHF modeling efforts may be classified into three general categories: boundary layer separation models, bubble crowding models and sublayer dryout models. All three types of models are based on conditions that promote heater surface dryout, but differ in the physical description of the CHF triggering mechanism.

Boundary layer separation models are based on predicting the hydrodynamic conditions that cause the bulk liquid flow to separate from the heater surface, leaving the downstream heater surface dry. Kutateladze and Leont'ev [1] studied flow separation in an adiabatic tube with the aid of dye injection normal to the wall. Tong [2] examined liquid separation from a heater surface during flow boiling in a concentric annulus. In both cases, the bulk liquid separated from the heater surface when the rate of fluid flow normal to the wall (due to boiling or injection) reached a critical value. Kutateladze and Leont'ev, Tong and Baines *et al.* [3] all identified boundary layer separation as the trigger condition in modeling CHF. Boundary layer separation models have lost general acceptance because of observations

such as those of Fiori and Bergles [4], Mattson *et al.* [5], and Hino and Ueda [6, 7]. In these studies, CHF was observed to occur on a localized basis as a result of isolated liquid–vapor interactions and not by the complete separation of the liquid flow from the heater surface.

Bubble crowding CHF models focus on the liquid–vapor exchange near the heater surface. Hebel *et al.* [8] identified the CHF trigger mechanism as the conditions for which departing bubbles obstruct the flow of liquid towards the heater surface. Weisman and Pei [9] postulated that CHF commences when the turbulent fluctuations in the liquid flow near the wall become too weak to transport liquid through the bubbly layer. At CHF, the critical void fraction in the bubbly layer was estimated from experimental bubble size and shape measurements to be 82%; however, other researchers have measured void fractions at CHF ranging from as low as 30% to as high as 95% depending on flow velocity, pressure and subcooling [10]. The validity of the bubble crowding models is, therefore, questionable in view of both the critical void fraction assumption and the empiricism required to determine the turbulent exchange in the bubbly layer.

Unlike the bubble crowding models, the sublayer dryout CHF models treat the liquid–vapor exchange on a more localized basis by performing energy balances over discrete surface areas. Gaertner [11] observed such a liquid sublayer beneath coalescent bubbles in pool boiling as did Fiori and Bergles [4] in

† Present address: Cummins Engine Company, Columbus, IN 47202, U.S.A.

‡ Author to whom all correspondence should be addressed.

Lee and Mudawar [10] proposed a mechanistic sublayer dryout model which eliminated the need for much of the empiricism found in previous flow boiling CHF models. An energy balance was written for a liquid sublayer trapped beneath a discrete elongated bubble. The length of the elongated bubble was assumed equal to the Helmholtz wavelength based upon the bubble rise velocity and liquid velocity, since bubbles which are longer than the Helmholtz wavelength become unstable and break into shorter bubbles. For bubbles to remain in the vicinity of the heater surface, a reaction force must oppose the outward vapor momentum flux from the evaporating sublayer. The sublayer thickness was modeled by performing a momentum balance in a direction normal to the heater surface. The vapor momentum flux into the elongated bubble was balanced by an opposing radial hydrodynamic force generated by bubble rotation and relative linear motion with respect to the mean liquid flow, known as the Magnus effect. Unlike most prior models, the CHF analysis proposed by Lee and Mudawar is theoretically based, requiring only a single empirical constant. Also, it closely predicts several well known CHF data bases over wide ranges of flow and pressure conditions.

Recently, Katto [16, 17] attempted to remove some of the objections to the Haramura and Katto model by employing essentially the same theoretical model constructed by Lee and Mudawar. An energy balance was written over discrete bubble lengths determined by the Helmholtz instability for a stationary liquid sublayer and an elongated bubble moving at a fraction of the two-phase flow velocity. Three empirically-based relations were required to model the bubble slip velocity, one for void fractions between 0.25 and 0.70, a second between 0 and 0.25 and a third for highly subcooled flow. The sublayer thickness was indirectly modeled using a correlation for pool boiling, removing many of the attractive theoretical features of the Lee and Mudawar model, that the Katto model was based upon.

The above review reflects both the complexity of CHF and the disagreement among investigators on the trigger mechanism for CHF. One reason for this confusion is the scarcity of near-wall microscopic observations which are essential to depicting the true nature of liquid-vapor exchange at CHF. Such observations are paramount ingredients in the construction of any CHF model. Part 1 of this study [18] served to provide detailed observations which are used in the present paper to develop a new theoretically-based, mechanistic model for flow boiling CHF.

2. CHF OBSERVATIONS

The CHF model is built upon a mathematical representation of the observed liquid-vapor exchange mechanism reported in Part 1 of this study [18]. As described in Part 1, a vapor wave was observed to cover the heater surface at heat fluxes above approxi-

mately 90% of CHF. Liquid was supplied to the heater surface though the wavy vapor layer at minimum contact points, wetting fronts, causing wetting and vigorous boiling.

Figure 1(a) shows a schematic representation of the vapor wave at approximately 99% of CHF, known hereafter as CHF (–), illustrating the general wetting front formation and propagation. Wetting fronts are formed when the liquid-vapor interface becomes unstable, forcing the interface to touch the heater surface. Wetting fronts were observed to be established consistently at the same distance, z^* , from the leading edge of the heater as illustrated by the wetting front labeled 1 corresponding to $t = 0$. The next depression in the interface could not establish a wetting front at a later time corresponding to $t = \lambda^*/2c$, because vapor generated by the boiling of liquid deposited earlier by wetting front 1 pushes away the interface. Without a resupply of liquid, the upstream wetting front begins to recede, $t = 3\lambda^*/2c$, as boiling consumes part of the liquid sublayer. At a later time, the heater surface becomes dry directly beneath the wavy interface at $z = z^*$ and this allows the interface to touch the dry heater surface at the upstream position marked +1 corresponding to $t = \lambda^*/c$. A new wetting front is then established at $z = z^*$ and the sequence is re-initiated, producing wetting fronts separated by a wavelength λ^* . This sequence is periodic, repeating itself at λ^*/c intervals, where c is the propagation speed of the interfacial wave.

A small increase in power above CHF, referred to hereafter as CHF (+), produced sufficient vapor momentum perpendicular to the heater surface at $z = z^*$ to lift the first wetting front away from the surface, Fig. 1(b). Ultimately, all wetting fronts are lifted from the surface except for a small region of persistent wetting remaining at the leading edge of the heater.

A summary of the key observations, based on Part 1 of this study, are given for reference in constructing the CHF model.

1. Continuous wetting was observed along the leading portion of the heater up to some distance z^* .
2. Wetting fronts were established repeatedly at approximately the same distance, z^* , downstream from the leading edge of the heater.
3. Wetting fronts maintained an approximately equal spacing, λ^* .
4. Intense boiling was observed in the wetting fronts while the other portions of the heater surface remained dry.
5. Wetting front lengths appeared to be preserved as the wetting fronts propagated downstream.
6. Wetting fronts propagated at a speed equal to the interfacial wave speed, c .
7. The liquid-vapor interface lost curvature at wetting fronts during the transition from CHF (–) to CHF (+) (this observation will be discussed in detail later in this paper).
8. CHF (+) was initiated by the separation of the

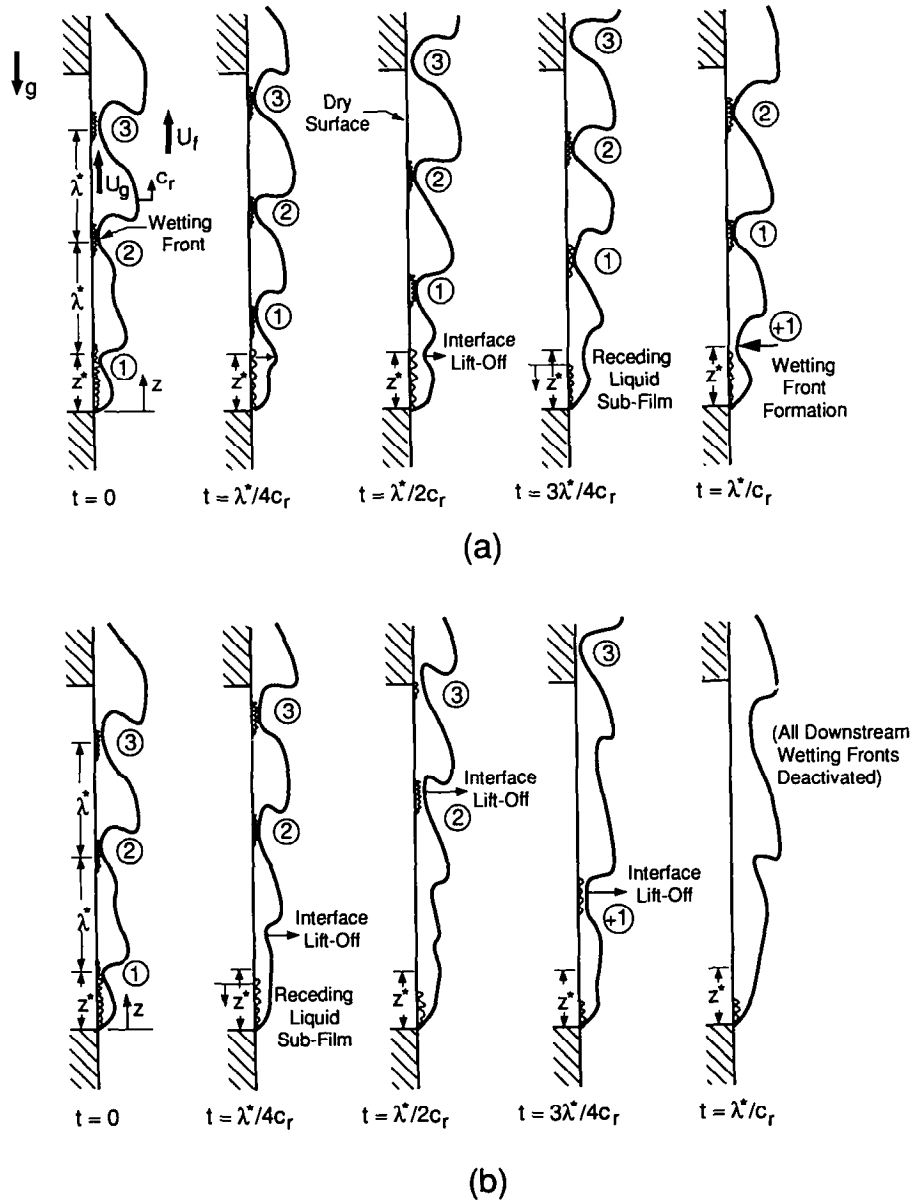


FIG. 1. Illustration of a complete cycle of events observed at (a) 99% CHF and (b) 101% CHF.

upstream wetting front due to vigorous boiling at the surface.

3. CHF MODEL

The CHF model is based on four sub-models which describe the individual mechanisms leading to the lifting of the liquid-vapor interface. First, an interfacial instability analysis is used to describe the spacing of the wetting fronts and pressure force created by interfacial curvature. Second, a separated flow model is used to predict the local mean values of liquid velocity, U_r , vapor velocity, U_g , and vapor layer thickness, δ . Third, an energy balance is written for the heater surface, relating the average heat flux at CHF to the

heat flux concentrated in the wetting fronts as they transverse the heater length. Fourth, the CHF trigger mechanism is determined by calculating the heat flux required to generate a momentum flux of vapor effusion from wetting fronts that equals the new force exerted on the interface due to curvature.

3.1. Instability of the liquid-vapor interface

Interfacial instability observations were illustrated in Fig. 1 and reported in Part 1 of this study [18]. The spacing of wetting fronts and the pressure force exerted upon the interface may be predicted using classical instability theory [19, 20] by invoking the assumptions of incompressibility and inviscid flow.

The pressure difference generated by interfacial curvature is given by equation (1).

$$P_r - P_g = -\rho_r k (c - U_r)^2 \frac{\cosh k (H_r - \eta)}{\sinh k H_r} \eta - \rho_g k (U_g - c)^2 \frac{\cosh k (H_g + \eta)}{\sinh k H_g} \eta - (\rho_r - \rho_g) g_n \eta. \quad (1)$$

Equating the pressure force exerted upon the interface to the surface tension force yields

$$k \rho_g (U_g - c)^2 \coth (k H_g) + k \rho_r (c - U_r)^2 \coth (k H_r) = -g_n (\rho_r - \rho_g) + \sigma k^2. \quad (2)$$

The wave speed, c , in equations (1) and (2) has both real and imaginary components, c_r and c_i , respectively. The real component determines the wave propagation speed while the imaginary component defines conditions which promote interfacial instability.

$$c_r = \frac{\rho_g U_g \coth (k H_g) + \rho_r U_r \coth (k H_r)}{\rho_g \coth (k H_g) + \rho_r \coth (k H_r)} \quad (3)$$

$$-c_i^2 k^2 = \frac{\sigma k^3}{[\rho_g \coth (k H_g) + \rho_r \coth (k H_r)]} - \frac{\rho_g \rho_r \coth (k H_g) \coth (k H_r) [U_g - U_r]^2 k^2}{[\rho_g \coth (k H_g) + \rho_r \coth (k H_r)]^2} - \frac{g_n k (\rho_r - \rho_g)}{[\rho_g \coth (k H_g) + \rho_r \coth (k H_r)]}. \quad (4)$$

When $-c_i^2 k^2$ becomes negative, an interfacial disturbance having a wave number $k_c = 2\pi/\lambda_c$ will grow and approach the heater surface. Equation (4) shows surface tension is the stabilizing force opposing the destabilizing effects of both the inertial force and the body force. Longer wavelengths will become unstable first. However, close to the leading edge, these wavelengths cannot exist because their lengths are larger than the corresponding stream-wise location. Conditions become more favorable for interfacial instability further downstream as the phase velocity increases and longer wavelengths can be accommodated.

A difficulty arises in identifying the first wetting location, z^* , shown in Fig. 1(a). At the leading edge of the heater, the vapor velocity is smaller than the liquid velocity, but further downstream the trend reverses at some location $z = z_o$. In the case of vertical flow, $g_n = 0$ and all wavelengths would be stable at $z = z_o$. Establishing a wetting front before $z = z_o$, is possible but unlikely since z_o is typically less than 0.65 mm (approximately 5% of the heater length), and the velocity difference is relatively small. Therefore, the first opportunity for the interface to contract the heater surface occurs at a distance

$$z^* = z_o + \lambda_c. \quad (5)$$

Since upstream wetting was observed to occur every other cycle (due to the receding wetting zone illus-

trated in Fig. 1(a)), wetting front spacing is modeled as twice the critical wavelength,

$$\lambda^* = 2\lambda_c. \quad (6)$$

3.2. Separated flow model

Determining z^* and λ_c requires knowing the local values of U_r and U_g . A one-dimensional separated flow model was developed to predict U_r , U_g and δ by writing mass and momentum conservation equations for both the liquid and vapor layers, along with a surface energy boundary condition. Modeling the hydrodynamics of the separated two-phase flow was complicated by the transient nature arising from the waviness of the liquid-vapor interface. To make the analysis more tractable, the model predicted values of U_r and U_g based upon a time-averaged thickness, δ , of a smooth vapor layer, and a time-averaged heat flux, which was assumed uniform over the heated surface. Details of the separated flow model are summarized in Appendix A.

3.3. Surface energy balance

The boiling surface heat flux, q_s , is actually a function of both time and space due to the motion of wetting fronts. Hence, a Lagrangian description is necessary for describing the energy balance at the heater surface. An energy balance, written over a control volume extending from the heater surface in a direction normal to the heater surface to a depth in the heater large enough to allow a uniform heat flux boundary condition to be imposed, gives

$$\int_0^\tau \int_0^L q_s dz dt = q_m \tau L. \quad (7)$$

The period, τ , in equation (7) corresponds to a complete cycle starting from the formation of a wetting front near the leading edge of the heater, Fig. 1(a), to the time just before the next wetting front touches the heater surface at the same position, Fig. 1(e).

$$\tau = \frac{\lambda^*}{c_r} = \frac{2\lambda_c}{c_r}. \quad (8)$$

Two separate boiling zones were observed on the heater surface. A continuous boiling zone persisted near the leading edge of the heater whereas downstream locations experienced dry periods followed by intermittent periods of vigorous boiling in the wetting fronts. The heat flux in the upstream wetting zone is assumed equal to q_m since steady boiling precluded any heat storage or release of high heat fluxes. The continuous and intermittent wetting zones are modeled by separating the spatial integral in equation (7) into two terms.

$$q_m L \tau = \int_0^\tau \int_0^{z^*} q_m dz dt + \int_0^\tau \int_{z^*}^L q_s dz dt = q_m z^* \tau + \int_0^\tau \int_{z^*}^L q_s dz dt \quad (9)$$

where z^* is the extent of the continuous wetting zone at the leading edge. Equation (9) can be separated into the sum of integrals corresponding to each wetting front in contact with the heater surface.

$$q_m = \frac{c_f/2\lambda_c}{L-z^*} \left(\int_0^\tau \int_{z^*}^L q_{s,1} dz dt + \dots + \int_0^\tau \int_{z^*}^L q_{s,n-1} dz dt + \int_0^\tau \int_{z^*}^L q_{s,n} dz dt \right) \quad (10)$$

where $q_{s,1}, q_{s,2}, \dots, q_{s,n-1}, q_{s,n}$ are the surface heat fluxes corresponding to wetting fronts 1, 2, n , respectively. The number of wetting fronts, n , is specified by the relation

$$n = INT((L-z^*)/\lambda^*) + 1 \quad (11)$$

where INT is a function that takes the integer of the argument truncating the remainder.

At any given location, z , the local heat flux, q_s , is assumed equal to a concentrated heat flux, q_l , if the wetting front is present, otherwise $q_s = 0$ corresponding to the dry surface. The concentrated heat flux, which is larger than q_m , is modeled (see next section) as the heat flux required to lift the first wetting front at $z = z^*$ from the heater surface. This is a sufficient and necessary condition for triggering CHF since all downstream wetting fronts and wetting fronts yet to form will be deactivated once the upstream front is lifted from the surface. Visual observation in the present study revealed the liquid-vapor interface assumed a sinusoidal shape and boiling takes place over a fraction $b = 1/4$ of the wavelength λ^* (see ref. [18]). This fraction encompasses interfacial distances from the heater surface which are smaller than about 30% of the interfacial amplitude. A value of b equal to $1/4$ was, therefore, used to estimate the span of wetting fronts in modeling CHF for all flow velocities. Similar approaches have been used in previous theoretically-based CHF models to predict interfacial instability features [12].

Each integral in equation (10) is evaluated sep-

arately by considering the travel time and contact length for each wetting front. Depending upon the values of L, λ^* and b , one of three downstream wetting front configurations is possible as illustrated in Fig. 2. The last wetting front, n , will either extend beyond the trailing edge, with the center of the wetting front falling upstream, case (I), or downstream, case (II), off the trailing edge, or will be fully on the heater surface, case (III). Equation (12) identifies the distance between the center of wetting front n and the trailing edge, which may be used to infer which wetting front configuration is present.

$$\psi = L - z^* - (n-1)\lambda^* \quad (12)$$

Surface energy balances written for downstream wetting fronts must accommodate the transition from the heater surface to the insulated channel wall as wetting front n travels past the trailing edge. Details of these energy balances are presented in Appendix B.

3.4. Lift-off heat flux

The lift-off heat flux, q_l , was modeled as the heat flux required to produce a momentum flux of vapor that exceeds the pressure difference created by the curvature in the wavy liquid-vapor interface. Flow visualization at CHF revealed a liquid-vapor interface being lifted from the boiling surface, a condition identified earlier as the trigger mechanism for CHF. This condition is modeled by examining the momentum balance in a direction normal to the heater surface, including the effects of pressure difference, surface tension and the momentum flux of vapor departing from the boiling surface.

Figure 3(a) shows the liquid-vapor interface as it approaches the heater surface at $z = z^*$ to form the first wetting front. The differential control volume shown identifies a balance between the surface tension force and the net force due to the pressure difference across the interface.

$$P_r - P_g = F''_{\sigma_n, \text{before}} \quad (13)$$

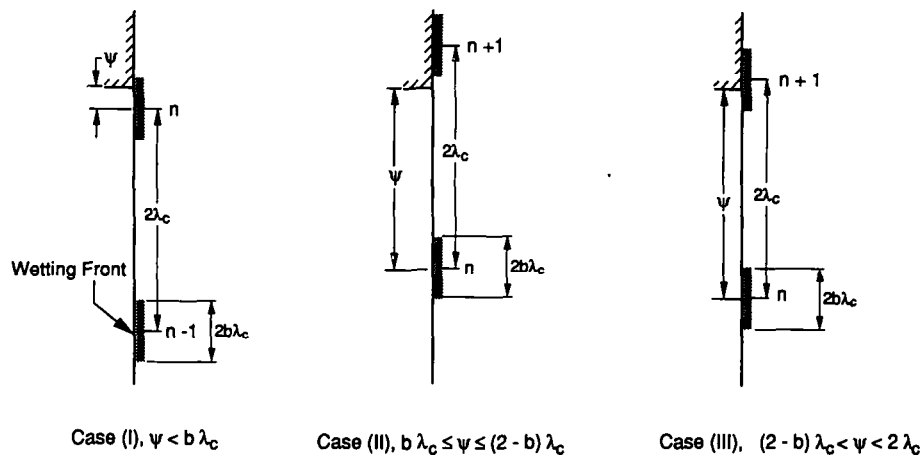


FIG. 2. Downstream wetting front configurations.

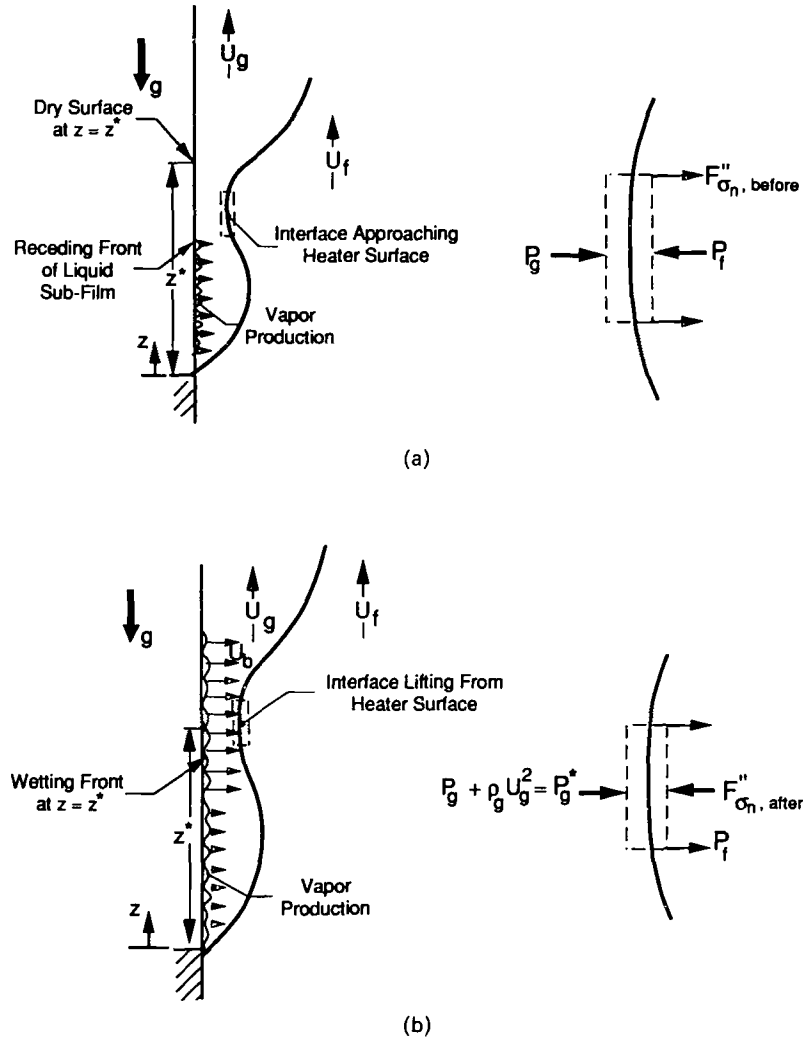


FIG. 3. (a) Interface approaching dry heater surface at $z = z^*$ just prior to wetting. (b) Lifting of interface after wetting the heater surface at $z = z^*$.

where $F''_{\sigma_n, \text{before}}$ is the component of surface tension force normal to the interface for a heater surface which is dry at $z = z^*$, divided by a small interfacial area near the center of contact. Vapor motion in the control volume at this instant is assumed to be parallel to the heater surface in the absence of boiling at $z = z^*$. After making contact and wetting the heater surface, a momentum flux due to vapor effusion is generated perpendicular to the heater surface, which alters the previously established interfacial mechanical balance. If a slight increase in heater power causes the momentum flux to exceed the net force on the interface due to the previously stable CHF(-) condition, the interface will be lifted from the heater as shown in Fig. 3(b). Pressure on the vapor side of the interface must now assume a higher value, P_g^* , equal to the sum of the vapor layer pressure, P_g , and the momentum flux generated by boiling in the wetting front.

$$P_g^* = P_g + \rho_g U_b^2 \quad (14)$$

where U_b is the average velocity of vapor perpendicular to the surface. The new force balance becomes

$$P_f - (P_g + \rho_g U_b^2) = F''_{\sigma_n, \text{after}} \quad (15)$$

where $F''_{\sigma_n, \text{after}}$ is the component of surface tension force normal to the interface following wetting front lift-off, divided by a small interfacial area near the center of contact. Combining equations (13) and (15) yields,

$$\rho_g U_b^2 = (P_f - P_g) - F''_{\sigma_n, \text{after}} = F''_{\sigma_n, \text{before}} - F''_{\sigma_n, \text{after}} \quad (16)$$

Figure 4 shows the curved interface above a wetting front and, a few milliseconds later, the vapor momentum flux lifting the flattened interface away from the heater surface. Therefore, the term $F''_{\sigma_n, \text{after}}$ in equation (16) may be neglected due to the infinite radius of curvature precluding any surface tension effects. Once the interface starts lifting, the vapor and liquid layer pressures are altered by changing stream-line curva-

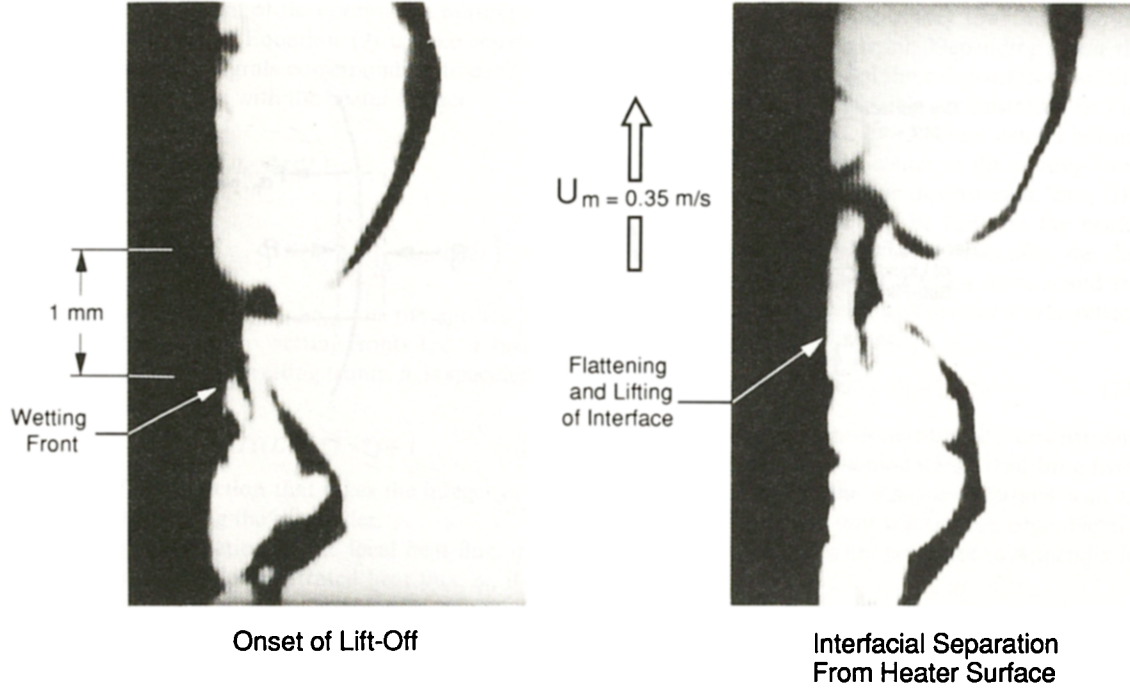


FIG. 4. Flattening of interface at CHF(+) following separation from heater surface ($U_m = 0.35 \text{ m s}^{-1}$, $q_m = 27.0 \text{ W cm}^{-2}$).

ture. With a reduction in stream-line curvature following lift-off, the vapor momentum flux becomes increasingly larger than the net pressure force, which accelerates the interfacial lift-off even further. Hence, the trigger condition for interfacial lift-off at CHF should correspond to the point of initial separation of the interface from the heater surface. Realizing that $F''_{\sigma_m, \text{after}}$ is negligible immediately following lift-off, equation (16) yields

$$\rho_g U_b^2 = P_r - P_g. \quad (17)$$

An expression for $(P_r - P_g)$ can be written using a relation derived from the interfacial instability analysis, equation (1), where $H_r (= H - \delta)$, H_g , U_r and U_g are determined from the separated flow model given in Appendix A. The velocity differences, $(U_g - c)$ and $(c - U_r)$ were calculated using the real component of wave velocity, c_r , predicted from equation (3). The local interfacial displacement, η , was determined from a sinusoidal shape assumed in the instability analysis with an amplitude equal to δ and wavelength equal to $2\lambda_c$ based on conditions at $z = z^*$.

The pressure difference increases from zero at $\eta = 0$ to its maximum positive value at $\eta = -\delta$, the point of contact with the heater surface. Figure 5 shows the local pressure difference across the interface at CHF predicted from equation (1) as a function of distance measured from the center of the wetting front for $q_m = 37.0 \text{ W cm}^{-2}$ and $U_m = 1.0 \text{ m s}^{-1}$. Since the pressure difference predicted at $\eta = -\delta$ is a local maximum, the pressure difference used in the force balance was calculated by averaging the normal component of pressure over the length of the wetting front.

The term $\rho_g U_g^2$ in equation (17) couples the hydro-

dynamic flow conditions (i.e. U_r , U_g , and δ) to the applied heat flux. The vapor velocity perpendicular to the heater surface can be related to the lift-off heat flux, q_l , by the expression

$$U_b = \frac{q_l}{\rho_g h_{fg} \left(1 + \frac{c_{p,r} \Delta T_{\text{sub}}}{h_{fg}} \right)}. \quad (18)$$

Combining equations (17) and (18) yields

$$q_l = \rho_g h_{fg} \left(1 + \frac{c_{p,r} \Delta T_{\text{sub}}}{h_{fg}} \right) \left(\frac{P_r - P_g}{\rho_g} \right)^{1/2}. \quad (19)$$

4. RESULTS

An iterative procedure is required to reach a convergent solution because of the coupling between the lift-off heat flux, interfacial instability analysis, separated flow model and the surface energy balance. The iteration begins for a specified U_m by guessing the value for q_m . The separated flow model uses this value to predict U_f , U_g and δ . Knowing the values of these parameters, the stability analysis determined λ_c , z_o and $(P_r - P_g)$. The lift-off heat flux is based upon the calculated $(P_r - P_g)$. A surface energy balance is then written using the guessed q_m and the calculated q_l . Iteration continues until the guessed q_m equals the calculated q_m . Figure 6(a) shows the CHF model predictions match the experimental data with a 7.1% mean absolute error. Figure 6(b) compares the measured wavelengths (with the indicated error bars showing one standard deviation in the data) to the predicted wavelengths, $2\lambda_c$.

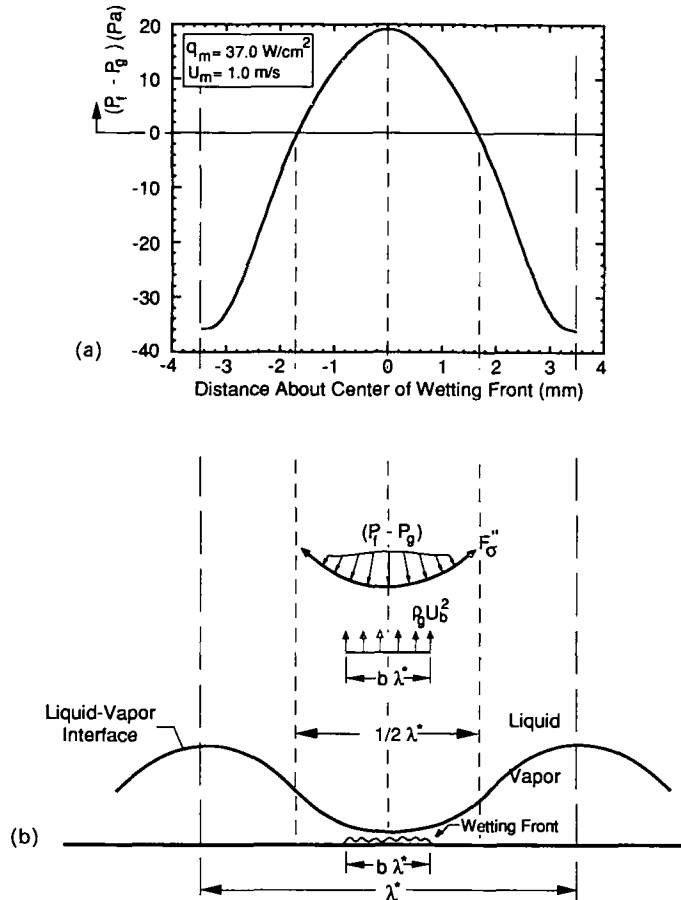


FIG. 5. (a) Interfacial pressure difference over one wavelength, λ^* . (b) Effect of vapor momentum on pressure distribution due to boiling over a fraction, b , of the wavelength.

Table 1 compares measured to predicted values of CHF, wavelength, number of wetting fronts and lists the downstream wetting front configuration. For velocities below $U_m = 1.00 \text{ m s}^{-1}$, the CHF model predicts two wetting fronts maintain contact with the heater surface, characterized by case (II) given in Fig. 2, and shows reasonable agreement with the photographs reported in Part 1 of this study. A transition from a case (II) to a case (III) downstream configuration is predicted at a velocity of $U_m = 1.0 \text{ m s}^{-1}$, resulting in an upstream, an interior and a downstream wetting front. At velocities greater than $U_m = 1.0 \text{ m s}^{-1}$, the downstream wetting front configuration follows case (II) and three wetting fronts are predicted. Smaller wavelengths were observed and predicted at high velocities, although there appears to be larger disagreements perhaps resulting from a greater difficulty in clearly discerning interfacial features. Nonetheless, the agreement is fair and supports the overall modeling approach, considering the complex nature of the interfacial waviness.

The results of Table 1 provide some insight into many previously reported macroscopic descriptions of CHF. In a study of flow boiling from a short heater in a rectangular channel, Mudawar and Maddox [15]

observed significant differences in CHF at high flow velocities as compared to low velocities. At low velocities, $U_m \ll 2 \text{ m s}^{-1}$, a large vapor blanket seemed to engulf the heater surface at CHF, while at high velocities, $U_m \gg 2 \text{ m s}^{-1}$, smaller, discrete blankets seemed to propagate along the heater surface prior to dryout. The present study proves the observed blankets are actually perturbations in the liquid-vapor interface. Low velocities produce large wavelengths which may engulf over one half the heater length (which was equal, 1.27 mm, to the heater used in the present study), taking the shape of a single blanket. On the other hand, higher flow velocities promote wetting in several fronts separated by relatively short wavelengths.

5. CONCLUSIONS

A new understanding of the CHF mechanism in flow boiling has emerged from near-wall microscopic observations of heater surface dryout. These observations were employed in the development of a new theoretical CHF model. Key findings from the present study are as follows:

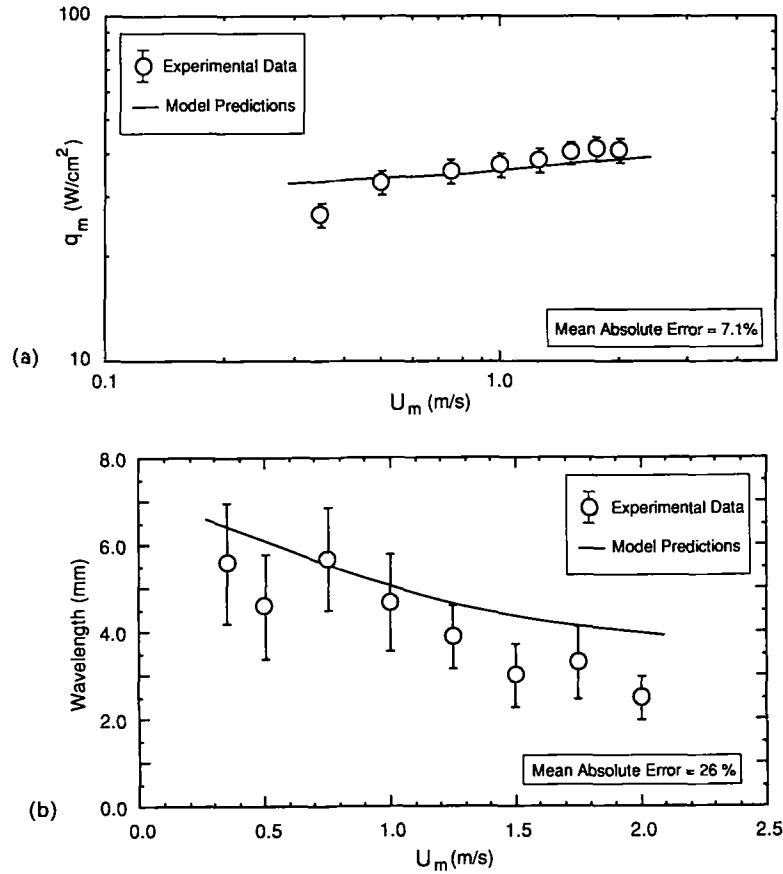


FIG. 6. Comparison of model predictions to experimental data of (a) CHF and (b) wavelength ($2\lambda_c$).

1. Bubbles which form at the heater surface coalesce into a wavy vapor layer at heat fluxes well below CHF. Hydrodynamic instability of the liquid-vapor interface promotes the formation of wetting fronts at points of liquid contact with the heater surface. As the heat flux approaches CHF, boiling persists in the wetting fronts while the surrounding surface regions become dry. The distance between consecutive wetting fronts and the propagation speed of the wetting fronts can be predicted from classical instability theory coupled with a simple separated flow model of the vapor layer.

2. The CHF trigger mechanism is the separation of the liquid-vapor interface from the heater surface at the location of the upstream wetting front due to intense vapor effusion normal to the heater surface. The upstream interfacial separation concentrates the heat removal from the remaining wetting fronts, causing a catastrophic cascading separation of the downstream wetting fronts and acceleration of the heater surface temperature excursion resulting from the ensuing dryout. The separation of the liquid-vapor interface from the heater surface is a result of the momentum of the effused vapor exceeding the net

Table 1. Comparison of model predictions to experimental data

U_m (m s ⁻¹)	$q_{m,exp}$ (W cm ⁻²)	$q_{m,model}$ (W cm ⁻²)	Measured wavelength (mm)	$2\lambda_c$ (mm)	z_o (mm)	z^* (mm)	Number of waves touching heater surface	Case number
0.35	26.5	33.9	5.64	6.4	0.00	3.2	2	(II)
0.50	33.0	34.2	4.6	6.1	0.10	3.1	2	(II)
0.75	35.5	35.1	5.66	5.6	0.20	2.9	2	(II)
1.00	37.0	36.1	4.67	5.1	0.30	2.7	3	(III)
1.25	38.3	37.1	3.94	4.7	0.40	2.5	3	(I)
1.50	40.3	37.6	3.02	4.4	0.50	2.4	3	(II)
1.75	41.3	38.4	3.28	4.2	0.60	2.4	3	(II)
2.00	40.8	38.8	2.50	4.0	0.65	2.4	3	(II)

pressure force normal to the heater surface caused by the curvature in the wavy interface.

3. The observed CHF trigger mechanism differs radically from the theory of dryout due to merging of vapor jets in the liquid sublayer [13]. In many ways, the present model captures several key macroscopic observations adopted by Kutateladze and Leont'ev [1] and Tong [2] in the development of boundary layer separation models. The present observations also lend validity to key assumptions in the Lee and Mudawar model [10], such as the determination of the characteristic length of a vapor cluster and the role of vapor momentum normal to the heater surface in restricting liquid inflow toward the surface. However, unlike previous models, the present model possesses the unique attributes of predicting the detailed interfacial features of the wavy vapor layer, and of incorporating the conservation of mass, momentum and energy in the near-wall region in a theoretically-based treatment.

REFERENCES

1. S. S. Kutateladze and A. I. Leont'ev, Some applications of the asymptotic theory of the turbulent boundary layer, *Proc. 3rd Int. Heat Transfer Conf.*, Chicago, Illinois, Vol. 3, pp. 1-6 (1966).
2. L. S. Tong, Boundary-layer analysis of the flow boiling crisis, *Int. J. Heat Mass Transfer* **11**, 1208-1211 (1968).
3. R. P. Baines, M. A. El Masri and W. M. Rohsenow, Critical heat flux in flowing liquid films, *Int. J. Heat Mass Transfer* **27**, 1623-1629 (1984).
4. M. P. Fiori and A. E. Bergles, Model of critical heat flux in subcooled flow boiling, *Proc. 4th Int. Heat Transfer Conf.*, Versailles, France, Vol. 6, pp. 354-355 (1970).
5. R. J. Mattson, F. G. Hammit and L. S. Tong, A photographic study of the subcooled flow boiling crisis in Freon-113, *ASME Paper 73-HT-39* (1973).
6. R. Hino and T. Ueda, Studies on heat transfer and flow characteristics in subcooled flow boiling—Part 1. Boiling characteristics, *Int. J. Multiphase Flow* **11**, 269-281 (1985).
7. R. Hino and T. Ueda, Studies on heat transfer and flow characteristics in subcooled flow boiling—Part 2. Flow characteristics, *Int. J. Multiphase Flow* **11**, 283-297 (1985).
8. W. Hebel, W. Detavernier and M. Decreton, A contribution to the hydrodynamics of boiling crisis in a forced flow of water, *Nuclear Engineering and Design* **64**, 443-445 (1981).
9. J. Weisman and B. S. Pei, Prediction of critical heat flux in flow boiling at low qualities, *Int. J. Heat Mass Transfer* **26**, 1463-1477 (1983).
10. C. H. Lee and I. Mudawar, A mechanistic critical heat flux model for subcooled flow boiling based on local bulk flow conditions, *Int. J. Multiphase Flow* **14**, 711-728 (1988).
11. R. F. Gaertner, Photographic study of nucleate pool boiling on a horizontal surface, *J. Heat Transfer* **87**, 17-29 (1965).
12. N. Zuber, M. Tribus and J. W. Westwater, The hydrodynamic crisis in pool boiling of saturated and subcooled liquid. In *International Developments in Heat Transfer*, ASME, pp. 230-236 (1961).
13. Y. Haramura and Y. Katto, A new hydrodynamic model of critical heat flux, applicable widely to both pool and forced convection boiling on submerged bodies in saturated liquids, *Int. J. Heat Mass Transfer* **26**, 389-399 (1983).
14. I. Mudawar, T. A. Incropera and F. P. Incropera, Boiling heat transfer and critical heat flux in liquid films falling on vertically-mounted heat sources, *Int. J. Heat Mass Transfer* **30**, 2083-2095 (1987).
15. I. Mudawar and D. E. Maddox, Critical heat flux in subcooled flow boiling of fluorocarbon liquid on a simulated electronic chip in a vertical rectangular channel, *Int. J. Heat Mass Transfer* **32**, 379-394 (1989).
16. Y. Katto, A physical approach to critical heat flux of subcooled flow boiling in round tubes, *Int. J. Heat Mass Transfer* **33**, 611-620 (1990).
17. Y. Katto, Prediction of critical heat flux of subcooled flow boiling in round tubes, *Int. J. Heat Mass Transfer* **33**, 1921-1928 (1990).
18. J. E. Galloway and I. Mudawar, CHF mechanism in flow boiling from a short heated wall—I. Examination of near-wall conditions with the aid of photomicrography and high-speed video imaging, *Int. J. Heat Mass Transfer* **36**, 2511-2526 (1993).
19. H. Lamb, *Hydrodynamics* (6th Edn) p. 371. Dover Publications, New York (1945).
20. L. M. Milne-Thompson, *Theoretical Hydrodynamics* (4th Edn), p. 409. Macmillan, New York (1960).
21. S. Levy, Prediction of two-phase annular flow with liquid entrainment, *Int. J. Heat Mass Transfer* **9**, 171-188 (1966).
22. I. Mudawar, Interfacial instabilities of air-driven liquid films, *Int. Comm. Heat Mass Transfer* **13**, 535-543 (1988).
23. J. E. Galloway, Critical heat flux enhancement in the presence of stream-wise curvature, Ph.D. Thesis, School of Mechanical Engineering, Purdue University, West Lafayette, Indiana (1991).

APPENDIX A. SEPARATED FLOW MODEL

The instability analysis employed in the present CHF model demanded knowledge of the stream-wise variations of liquid velocity, U_f , vapor velocity, U_g , and vapor layer thickness, δ . The vapor layer thickness increases in the stream-wise direction as more vapor is produced at the wall by evaporation and boiling of the liquid sublayer covering the upstream portion of the heater, or by boiling in the wetting fronts. An expression for the vapor velocity as a function of heater length, z , from the upstream edge of the heater surface is determined from a mass balance for a vapor layer control volume extending from the heater surface to the liquid-vapor interface.

$$U_g = \frac{1}{\delta} \frac{qz}{\rho_g(h_{fg} + c_{p,r}\Delta T_{sub})} \quad 0 < z < L \quad (\text{A.1})$$

where the inlet subcooling, ΔT_{sub} , is assumed to remain constant for $0 < z < L$. Downstream from the heater, the vapor velocity becomes

$$U_g = \frac{1}{\delta} \frac{qL}{\rho_g(h_{fg} + c_{p,r}\Delta T_{sub})} \quad z \geq L. \quad (\text{A.2})$$

Although not important to the CHF model development, equation (A.2) serves to validate predictions of pressure drop between the two pressure taps used in the channel.

The mass balance for a control volume extending over the entire channel cross section gives expressions for the liquid velocity.

$$U_f = \frac{U_m H}{H - \delta} - \frac{qz}{\rho_f(H - \delta)(h_{fg} + c_{p,r}\Delta T_{sub})} \quad 0 < z < L \quad (\text{A.3})$$

$$U_f = \frac{U_m H}{H - \delta} - \frac{qL}{\rho_f(H - \delta)(h_{fg} + c_{p,r}\Delta T_{sub})} \quad z \geq L. \quad (\text{A.4})$$

Thus, two sets of equations are available expressing U_g and U_f in terms of δ .

The momentum conservation equation, written first for

the vapor layer, Fig. A.1(a), and then for the entire channel cross-section, Fig. A.1(b), provides closure to the analysis. Summing forces and momentum fluxes over the vapor layer control volume shown in Fig. A.1(a) gives

$$\begin{aligned}
 & -\rho_g U_g^2 \delta s + \left[\rho_g U_g^2 \delta s + \frac{d}{dz} (\rho_g U_g^2 \delta) s \Delta z \right] \\
 & -\dot{m}_e'' U_i s \Delta z = P \delta s - \left(P \delta + \frac{d}{dz} (P \delta) \Delta z \right) s \\
 & + P \frac{d\delta}{dz} s \Delta z - \tau_g (s \Delta z + 2\delta \Delta z) - \tau_i s \Delta z - \rho_g g \delta s \Delta z. \quad (A.5)
 \end{aligned}$$

Boiling at the heater surface from the stationary liquid sublayer does not contribute to momentum in the stream-wise direction since vapor is ejected normal to the heater surface. Also, for the low subcooling conditions of the present study, interfacial evaporation had a negligible contribution to momentum transport in the stream-wise direction; therefore, the term $\dot{m}_e'' U_i s \Delta z$ shown in Fig. A.1 was set equal to zero.

Summing the pressure drop components across the entire channel cross section, Fig. A.1(b), gives

$$-\frac{dP}{dz} \equiv -\frac{dP}{dz} \Big|_F - \frac{dP}{dz} \Big|_G - \frac{dP}{dz} \Big|_A \quad (A.6)$$

where

$$-\frac{dP}{dz} \Big|_F \equiv \left[\frac{1}{H} + 2 \left(\frac{H-\delta}{Hs} \right) \right] \tau_f + \left(\frac{1}{H} + \frac{2\delta}{Hs} \right) \tau_g \quad (A.7)$$

$$-\frac{dP}{dz} \Big|_G \equiv \frac{\delta}{H} g \rho_g + \frac{(H-\delta)}{H} g \rho_f \quad (A.8)$$

$$-\frac{dP}{dz} \Big|_A \equiv \frac{1}{H} \left[\rho_f \frac{d}{dz} (U_i^2 (H-\delta)) + \rho_g \frac{d}{dz} (U_g^2 \delta) \right]. \quad (A.9)$$

The vapor layer thickness is adjusted until the pressure drop for the vapor layer determined from equation (A.5) equals the pressure drop calculated using equation (A.6).

Due to the large aspect ratio of the flow area for each phase, shear stresses τ_f and τ_g are modeled using friction factors f_f and f_g predicted from the Blasius correlation,

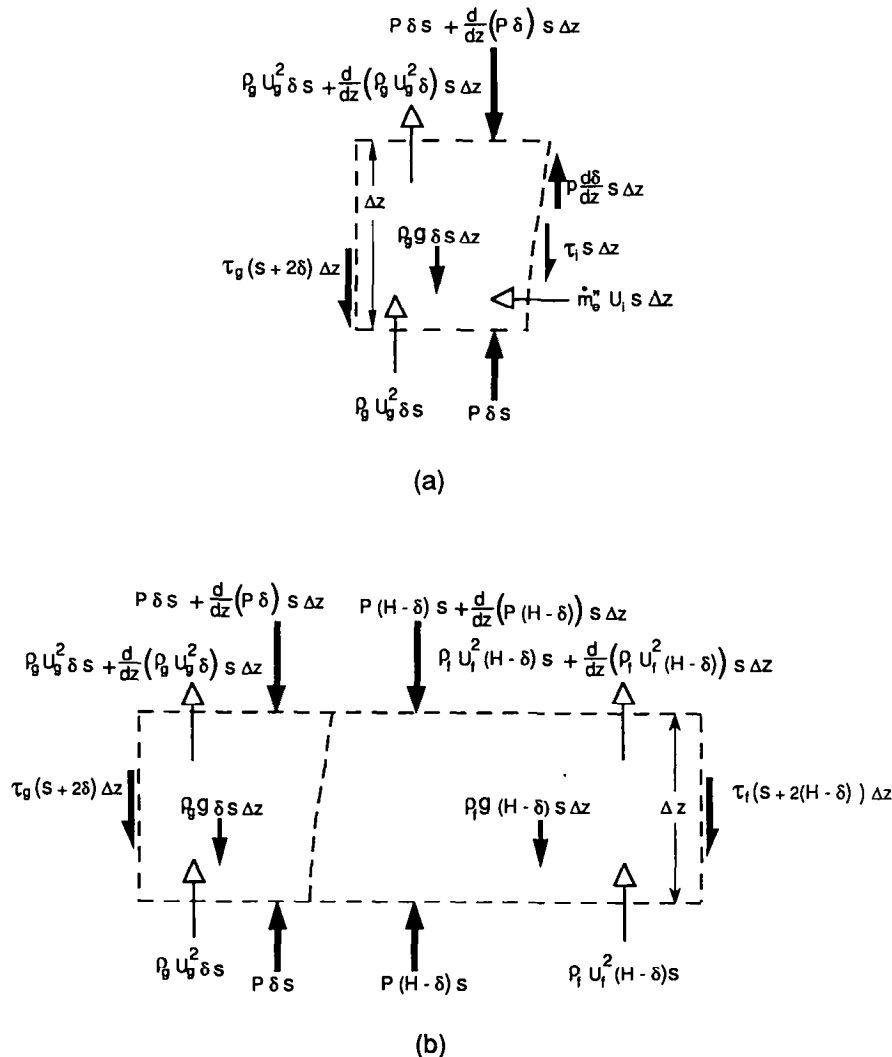


FIG. A.1. Separated flow control volume for (a) vapor layer and (b) full channel cross-section.

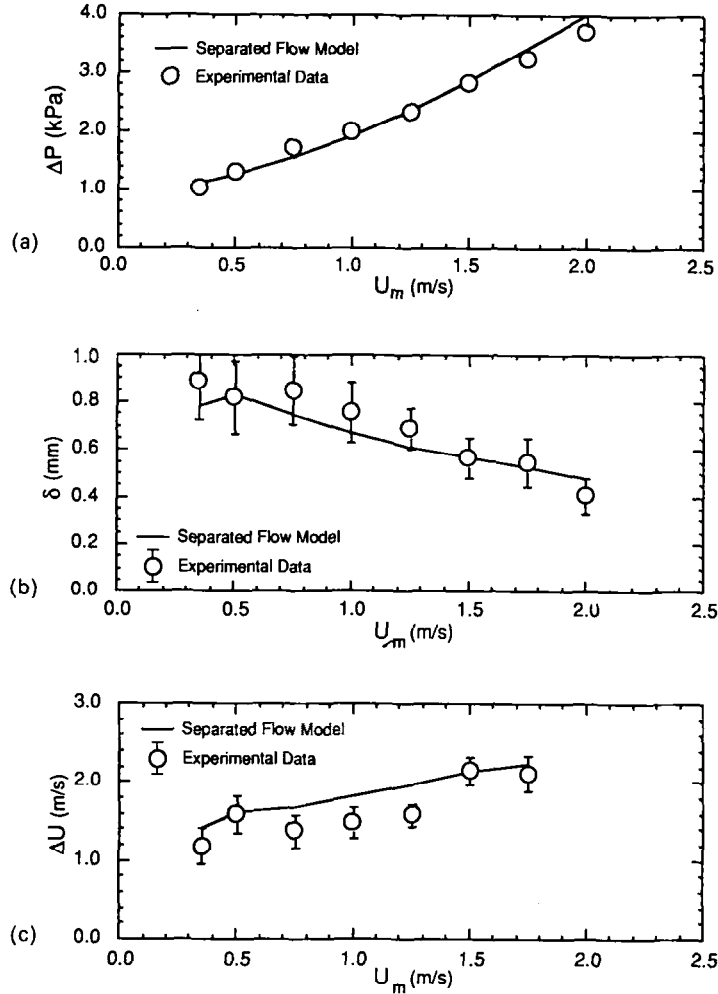


FIG. A.2. Comparison of separated flow model predictions and experimental data for (a) total pressure drop, (b) mean vapor layer thickness, and (c) relative velocity.

$f = 0.0791/Re_D^{0.05}$, based on the hydraulic diameter of each respective layer.

$$\tau_r = \frac{1}{2} f_r \rho_r U_r^2 \quad (\text{A.10})$$

$$\tau_g = \frac{1}{2} f_g \rho_g U_g^2. \quad (\text{A.11})$$

The interfacial shear stress, τ_i , is modeled using an interfacial friction coefficient, f_i , and the velocity difference across the interface.

$$\tau_i = \frac{1}{2} \rho_g f_i (U_g - U_r)^2. \quad (\text{A.13})$$

Levy [21] introduced a friction factor correlation for a wavy vapor-liquid interface in vertical annular flow. Based on the mean distances of the interface from the wall measured in the present study, Levy's correlation gives f_i values between 0.2 and 0.4. Mudawar [22] measured a friction factor of 0.2 for air flow over a solid sinusoidal wall having an amplitude to wavelength ratio of 0.37. There is, therefore, some uncertainty in estimating the interfacial friction factor for the flow conditions and shape of wave described in the present study. However, good agreement between the predicted and measured pressure drop was achieved using $f_i = 0.5$ which is higher than the two estimates perhaps due to intermittent contact of the interface with the wall. The frictional pressure drop contributes about 40% of the pressure drop in the vapor layer at a mean inlet velocity of 1.0 m s⁻¹. Judging from the strong influence of the interfacial

friction and the good agreement with the data, Fig. A.2, the value of 0.5 is recommended for conditions similar to those of the present study. It is important to point out that this value was determined from pressure drop data measured at fluxes smaller than CHF, and has no bearing on the derivation of the other sub-models used in predicting CHF.

APPENDIX B. SURFACE ENERGY BALANCE FOR DIFFERENT DOWNSTREAM WETTING FRONT CONFIGURATIONS

Downstream surface energy balances are written for the three cases shown in Fig. 2 assuming the heater length is sufficiently long such that wetting front $n-1$ does not contact the upstream continuous wetting zone. This limitation will be relaxed later for short heaters.

Figure B.1 shows the downstream wetting front propagation for case (I), $\psi < b\lambda_c$. The heat transferred to wetting fronts n and $n-1$ during one wetting period, τ , can be expressed as

$$\begin{aligned} & \int_0^\tau \int_{z^*}^L q_{s,n} dt dz + \int_0^\tau \int_{z^*}^L q_{s,n-1} dt dz \\ &= \int_0^{\tau_{1,n}} q_l (\psi + 1/2b\lambda^* - c_r t) dt \end{aligned}$$

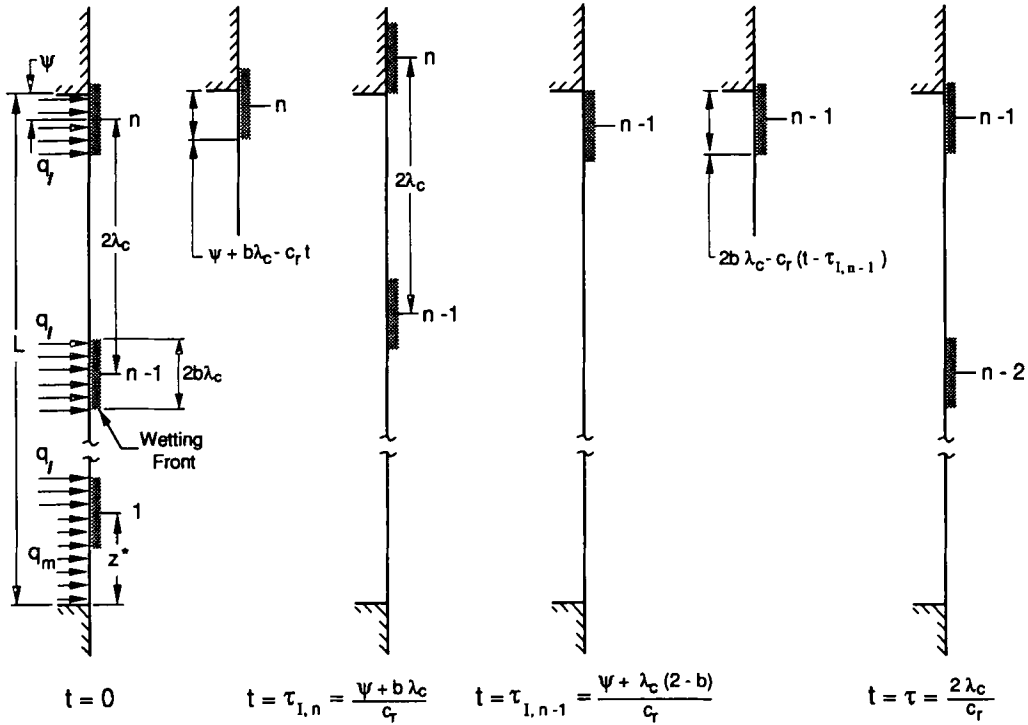


FIG. B.1. Positions of downstream wetting fronts during period τ for case (I), $\psi < b\lambda_c$.

$$\begin{aligned}
 & + \int_{\tau_{I,n}}^{\tau} 0 \, dt + \int_0^{\tau_{I,n-1}} q_1(b\lambda^*) \, dt \\
 & + \int_{\tau_{I,n-1}}^{\tau} q_1[b\lambda^* - c_r(t - \tau_{I,n-1})] \, dt \\
 & = \frac{q_1}{c_r} (\psi b\lambda^* + b\lambda^{*2}) \\
 & = \frac{q_1}{c_r} (2\psi b\lambda_c + 4b\lambda_c^2). \tag{B.1}
 \end{aligned}$$

For short heaters, wetting front $n-1$ overlaps the upstream continuous wetting zone and the downstream energy balance, equation (B.1), must be modified by subtracting the term

$$\int_0^{1/2b\lambda_c/c_r} q_1(\frac{1}{2}b\lambda_c - c_r t) \, dt = \frac{q_1}{8c_r} b^2\lambda^{*2} = \frac{q_1}{2c_r} b^2\lambda_c^2. \tag{B.2}$$

Long heaters are those having at least three wetting fronts centered on the heater surface for case (I) and at least two wetting fronts for cases (II) and (III). The surface energy balance is modeled by summing the heat dissipated from the first wetting front, the interior wetting fronts (which

contacted neither the upstream continuous wetting nor the trailing edge during period τ) and the downstream wetting fronts. Accounting for the overlap in the continuous wetting zone, the heat transferred to the first wetting front is given by

$$\begin{aligned}
 \int_0^{\tau} \int_{z^*}^L q_{s,1} \, dt \, dz & = \int_0^{1/2b\lambda^*/c_r} q_1(\frac{1}{2}b\lambda^* + c_r t) \, dt \\
 & + \int_{1/2b\lambda^*/c_r}^{\tau} q_1(b\lambda^*) \, dt = \frac{q_1}{c_r} \left(b\lambda^{*2} - \frac{b^2}{8}\lambda^{*2} \right) \\
 & = \frac{q_1}{c_r} (4b\lambda_c^2 - \frac{1}{2}b^2\lambda_c^2). \tag{B.3}
 \end{aligned}$$

Each of the interior wetting front has a constant wetting length and the heat dissipated during period τ is equal to $4b\lambda_c^2 q_1/c_r$.

Surface energy balances similar to those of case (I) can also be derived for cases (II) and (III). Table B.1 summarizes the surface energy balances used to model CHF for both short and long heaters. Details of the derivations of these relations can be found in ref. [23].

Table B.1. Summary of critical heat flux relations for short and long heaters for which $z^* < L$

	Case (I) $\psi < b\lambda_c$	Case (II) $b\lambda_c \leq \psi \leq (2-b)\lambda_c$	Case (III) $(2-b)\lambda_c < \psi < 2\lambda_c$
Short heaters	$n = 2$ $q_m = \frac{\{2\psi b\lambda_c + 4b\lambda_c^2 - \frac{1}{2}b^2\lambda_c^2\}}{(L-z^*)(2\lambda_c)} q_1$	$n = 1$ $q_m = \frac{\{2\psi b\lambda_c - \frac{1}{2}b^2\lambda_c^2\}}{(L-z^*)(2\lambda_c)} q_1$	$n = 1$ $q_m = \frac{\{2\psi b\lambda_c - \frac{1}{2}b^2\lambda_c^2\}}{(L-z^*)(2\lambda_c)} q_1$
Long heaters	$n > 2$ $q_m = \{4b\lambda_c^2 - \frac{1}{2}b^2\lambda_c^2 + (n-3)4b\lambda_c^2 + 2\psi b\lambda_c + 4b\lambda_c^2\} \frac{q_1}{(L-z^*)(2\lambda_c)}$	$n > 1$ $q_m = \{4b\lambda_c^2 - \frac{1}{2}b^2\lambda_c^2 + (n-2)4b\lambda_c^2 + 2\psi b\lambda_c\} \frac{q_1}{(L-z^*)(2\lambda_c)}$	$n > 1$ $q_m = \{4b\lambda_c^2 - \frac{1}{2}b^2\lambda_c^2 + (n-2)4b\lambda_c^2 + 2\psi b\lambda_c\} \frac{q_1}{(L-z^*)(2\lambda_c)}$